applied sciences

MDPI

Article

Synthetic Aperture Radar Interferometry (InSAR) Ionospheric Correction Based on Faraday Rotation: Two Case Studies

Wu Zhu [1,*], Hyung-Sup Jung [2,*] and Jing-Yuan Chen [1]

[1] College of Geology Engineering and Geomatics, Chang'an University, Xi'an 710064, China; 2018126022@chd.edu.cn

[2] Department of Geoinformatics, The University of Seoul, Seoul 130743, Korea

* Correspondence: zhuwu@chd.edu.cn (W.Z.); hsjung@uos.ac.kr (H.-S.J.); Tel.: +86-29-82339261 (W.Z.); +82-2-6490-2892 (H.-S.J.); Fax: +86-29-82339261 (W.Z.); +82-2-6490-2884 (H.-S.J.)

Received: 27 August 2019; Accepted: 11 September 2019; Published: 15 September 2019

Abstract: Spaceborne synthetic aperture radar (SAR) imagery is affected by the ionosphere, resulting in distortions of the SAR intensity, phase, and polarization. Although several methods have been proposed to mitigate the ionospheric phase delay of SAR interferometry, the application of them with full-polarimetric SAR interferometry is limited. Based on this background, Faraday rotation (FR)-based methods are used in this study to mitigate the ionospheric phase errors on full-polarimetric SAR interferometry. For a performance test of the selected method, L-band Advanced Land Observation Satellite (ALOS) Phase Array L-band SAR (PALSAR) full-polarimetric SAR images over high-latitude and low-latitude regions are processed. The result shows that most long-wavelength ionospheric phase errors are removed from the original phase after using the FR-based method, where standard deviations of the corrected result have decreased by almost a factor of eight times for the high-latitude region and 28 times for low-latitude region, compared to those of the original phase, demonstrating the efficiency of the method. This result proves that the FR-based method not only can mitigate the ionospheric effect on SAR interferometry, but also can map the high-spatial-resolution vertical total electronic content (VTEC) distribution.

Keywords: radar interferometry; ionosphere; polarimetric synthetic aperture radar; Faraday Rotation

1. Introduction

Synthetic aperture radar (SAR) imagery has demonstrated its potential in the military and in civilian fields, such as ground deformation observation and computer vision systems [1–4]. However, a challenge to the SAR imagery, particularly with low-frequency SAR systems, is the influence of the ionosphere. When SAR signals propagate through the ionosphere, their phase and polarization change [5–8]. There are a number of studies about ionospheric influences on SAR and SAR interferometry (InSAR), such as ionosphere-induced Faraday rotation (FR) on linearly polarized polarimetric SAR data [9–13], ionosphere-induced interferometric phase errors and azimuth offsets on InSAR measurements [14–16], ionospheric effects on simulated P-band SAR imagery [17,18] and comprehensive investigation of this effect on SAR and InSAR [19–24]. Moreover, with increasing interest in the low-frequency SAR systems (e.g., L-band TerraSAR operated by German Aerospace Center (DLR), NASA-ISRO Synthetic Aperture Radar (NISAR) operated by National Aeronautics and Space Administration (NASA), and P-band Biomass monitoring mission for Carbon Assessment (BIOMASS) operated by European Space Agency (ESA), this effect has become more significant and limits the further development of advanced SAR techniques [5].

To correct ionospheric distortions on SAR and InSAR, several methods have been proposed by researchers. Schneider and Papathanassiou [25] discussed and proposed a method to estimate and compensate of ionospheric effects by means of coherent scatterers, which had a high spectral correlation and point-like scattering behaviour. Rosen et al. [24] proposed an ionospheric correction method based on a multi-frequency split-spectrum processing technique. This method exploited the dispersive nature of radar signals in estimating the ionospheric contribution. When topography, ground deformation and atmospheric errors were non-dispersive, the ionospheric effect was dispersive. Thus, the ionospheric effect could be separated by observations at two different frequencies. Several researchers have proved the feasibility of this method [26–30]. Another method called Delta-k, which is similar to the multi-frequency split-spectrum processing technique, employs subband processing in range to separate frequency dependence of ionospheric phase delay versus the frequency proportional dependence of topographic phase delay [5,6,31]. Meyer et al. [20] successfully developed a method to map the ionospheric structures using SAR interferograms. This method exploited the differences in sign between range group and phase delays caused by the ionosphere. A recent method aimed to use the approximate linear relationship between the azimuth gradient of ionospheric phase delay and azimuth pixel shift to correct the ionospheric effect on InSAR [14,15,32–36]. Several researchers tested the feasibility of this method. As a result, it was reported that the method was able to correct the ionospheric phase error on the interferogram.

As the most sensible magneto-ionic propagation effects, ionosphere-induced FR can be accurately estimated from the full-polarimetric SAR images, and consequently has been widely used to correct ionospheric effects on SAR and InSAR [9]. Freeman [37] outlined a step-by-step procedure to recover the true scattering matrix subject to FR. The method provided an effective method to calibrate the ionospheric distortion on full-polarimetric SAR images. From then on, intensive studies were carried out to calibrate the ionosphere-induced FR and radar system errors for L-band Advanced Land Observation Satellite (ALOS)/Phase Array L-band SAR (PALSAR) [38–42] and simulated P-band BIOMASS systems [43]. Due to the presence of speckle noise in single SAR images, ionospheric correction on SAR interferometry was easily contaminated by the noise when directly using FR-calibrated single SAR images. In this situation, Kim [44] converted the estimated FR distribution to the vertical total electronic content (VTEC) map, and then applied this map to correct the ionosphere-induced interferometric phase delay. Then, he analyzed the factors which may affect the performance of ionospheric correction on SAR interferometry, including ionospheric condition, underlying SNR, number of looks, and geomagnetic latitude. His results proved the feasibility of ionospheric correction on SAR interferometry by using the FR-based method. However, the limitation of his method is that there is the remarkable residual long-wavelength phase signal in the corrected interferogram. In order to evaluate the performance of the FR-based method and the azimuth offset method in practical applications, Zhu et al. [45] made an investigation using L-band polarimetric SAR data, and found that the FR-based method was more sensitive to the noise than the azimuth offset method. Meanwhile, it was found that both methods present the residual ionospheric phase error in the corrected interferogram.

To address limitations in the current ionospheric correction methods on SAR interferometry, an efficient FR-based method is employed to mitigate the ionospheric errors on full-polarimetric SAR interferometry. This method exploits the fact that ionospheric errors on an interferogram can be extracted based on the relationship between FR angles and VTEC (vertical total electronic content). Compared with the existing FR-based methods introduced in [44] and [45], the proposed method uses an integrated phase model, which can correct the ionospheric error as well as the residual ionospheric phase error caused by inaccurate parameters on SAR interferometry, and thus can improve the correction precision. The process is composed of three steps: (1) estimation of FR angles from full-polarimetric SAR images, (2) generation of VTEC maps from FR angles, and (3) joint correction of long-wavelength ionospheric phase errors on full-polarimetric interferograms. For performance testing of the proposed method, L-band ALOS/PALSAR full-polarimetric SAR images over high-latitude and low-latitude regions are processed. The FR angles and VTEC maps are estimated from SAR images,

and then ionospheric errors of full-polarimetric interferograms are calculated and corrected from VTEC maps.

2. Methods

Figure 1 shows the flowchart of the proposed method to mitigate the ionospheric phase error on full-polarimetric SAR interferometry. The scheme mainly involves three aspects: estimation of the FR angle from the measured scattering matrix, transformation of the FR angle to the VTEC distribution, and correction of ionospheric phase error. The detailed processing approaches are described below:

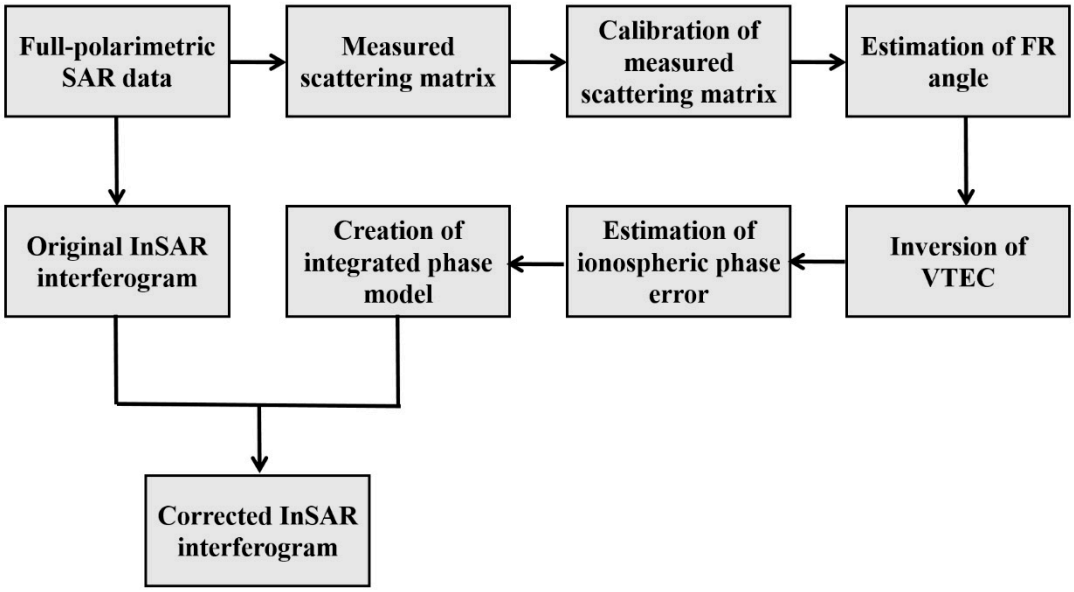

Figure 1. The flowchart of the proposed method. Synthetic aperture radar (SAR), SAR interferometry (InSAR), Faraday rotation (FR), vertical total electronic content (VTEC).

2.1. Estimation of the FR Angle from Full-Polarimetric SAR Data

For a linear polarization SAR system, the measured scattering matrix M can be written as [37]:

$$\begin{gathered} M = Ae^{j\Phi}R^T R_F S R_F T + N \\ M = \begin{bmatrix} M_{hh} & M_{vh} \\ M_{hv} & M_{vv} \end{bmatrix}, R_F = \begin{bmatrix} cos\Omega & sin\Omega \\ -sin\Omega & cos\Omega \end{bmatrix}, S = \begin{bmatrix} S_{hh} & S_{vh} \\ S_{hv} & S_{vv} \end{bmatrix}, \\ R^T = \begin{bmatrix} 1 & \delta_1 \\ \delta_2 & f_1 \end{bmatrix}, T = \begin{bmatrix} 1 & \delta_3 \\ \delta_4 & f_2 \end{bmatrix}, N = \begin{bmatrix} N_{hh} & N_{vh} \\ N_{hv} & N_{vv} \end{bmatrix}, \end{gathered} \tag{1}$$

where R_F is a one-way FR matrix; Ω is the FR angle; S is the true scattering matrix; R and T are the receiving and transmitting distortion matrices, respectively; f_1 and f_2 are the channel imbalance (the complex ratio of signals Vertical(V)/Horizontal(H) on receive and transmit, respectively); δ_1, δ_2, δ_3, δ_4 are the complex antenna crosstalk terms resulting from the incomplete isolation of H and V polarizations on transmit and receive; A is the overall gain of radar system, which is a function of radar range and elevation angle; $e^{j\Phi}$ corresponds to the round-trip phase delay and system-dependent phase effects on signal; and N is an additive noise term due to earth radiation, thermal fluctuations in the receiver and digitization noise [37]. A calibration technique applied to SAR data can estimate and correct the system-dependent terms of A, $e^{j\Phi}$, R and T in (1) [13]. Furthermore, filtering methods, such as boxcar, band-pass and low-pass filters, can be used to suppress the additive noise N. After these calibrations, the measured scattering matrix M can be reformed as given by:

$$M = R_F S R_F \tag{2}$$

After expanding (2) and invoking true backscatter reciprocity ($S_{hv} = S_{vh}$), the components of matrix M can be defined as:

$$\begin{aligned} M_{hh} &= S_{hh}cos^2\Omega - S_{vv}sin^2\Omega, \\ M_{vh} &= S_{hv} + (S_{hh} + S_{vv})sin\Omega cos\Omega, \\ M_{hv} &= S_{hv} - (S_{hh} + S_{vv})sin\Omega cos\Omega, \\ M_{vv} &= S_{vv}cos^2\Omega - S_{hh}sin^2\Omega. \end{aligned} \tag{3}$$

For cross-polarization, a nonzero FR angle means that the measured scattering matrix will not be invertible ($M_{vh} \neq M_{hv}$). Suppose that FR angle is the only error source and full-polarization SAR data is available, then the FR angle can be easily estimated from (3). A robust algorithm has been proposed to estimate the FR angle through circular polarization scattering matrix Z [9], as given by:

$$Z = \begin{bmatrix} Z_{RR} & Z_{RL} \\ Z_{LR} & Z_{LL} \end{bmatrix} = \begin{bmatrix} 1 & j \\ j & 1 \end{bmatrix} \times \begin{bmatrix} M_{hh} & M_{hv} \\ M_{vh} & M_{vv} \end{bmatrix} \times \begin{bmatrix} 1 & j \\ j & 1 \end{bmatrix} \tag{4}$$

$$Z_{LR} = M_{vh} - M_{hv} + j \times (M_{hh} + M_{vv}) \tag{5}$$

$$Z_{RL} = M_{hv} - M_{vh} + j \times (M_{hh} + M_{vv}) \tag{6}$$

From (3) and (4), FR angle Ω can be calculated by [9]:

$$\Omega = -\frac{1}{4} \times arg(Z_{RL} \times Z_{LR}^*), \text{ for } -\frac{\pi}{4} < \Omega < \frac{\pi}{4}. \tag{7}$$

where arg denotes the argument of a complex number and * represents the complex conjugate. From (7), it can be seen that estimation of the FR angle becomes a phase estimation problem, which is a fairly well-understood problem in radar polarization [46]. Further, a reduction in noise is required in order to increase the quality of FR angle estimation. Some filtering methods can be used for the reduction.

2.2. Inversion of VTEC Distribution from the FR Angle

The linearly polarized signal will experience a rotation of the polarization plane by an angle Ω when it propagates through the ionosphere layer. This angle is known as the FR angle [47]. The magnitude of FR angle Ω, for a wave of frequency f, traveling vertically one way through the ionosphere can be expressed as [48]:

$$\Omega = \frac{\left|e^3\right|}{8\pi^2 c\varepsilon_0 m^2} \cdot \frac{\overline{B \cdot \cos\theta \cdot \sec\phi} \cdot VTEC}{f^2} = \frac{2.365 \times 10^4 \cdot \overline{B \cdot \cos\theta \cdot \sec\phi} \cdot VTEC}{f^2} \tag{8}$$

where e and m are the charge and mass of an electron respectively; c is the speed of light; ε_0 is the permittivity of free space; B is the intensity of earth's magnetic field, which can be calculated from geomagnetic field data, such as International Geomagnetic Reference Field (IGRF) data; θ is the angle between the magnetic field and satellite pointing vector; ϕ is the SAR incidence angle; $\overline{B \cdot cos\theta \cdot sec\phi}$ is the magnetic field factor at a constant height (e.g., 400 km); and f is the radar frequency. Generally, the value of $\overline{B \cdot cos\theta \cdot sec\phi}$ depends on the geographic coordinates, orbit and imaging geometry of satellite, and can be calculated from [11]. Once the FR angle is determined by (7), VTEC is calculated by:

$$VTEC = \Omega \cdot \frac{f^2}{2.365 \times 10^4 \cdot \overline{B \cdot cos\theta \cdot sec\phi}} \tag{9}$$

2.3. Mitigation of Ionospheric Errors on SAR Interferogram

SAR signals travelling through the ionosphere layer are delayed along their paths by interactions with the free electrons. This delay leads to a group delay and a phase shift, which are equal in

magnitude, but opposite in sign. The ionosphere-induced phase shift φ_{ION} in a SAR interferogram corresponds to [22]:

$$\begin{aligned} \varphi_{ION} &\approx -\frac{2.675\times10^{-7}}{f} \cdot \frac{\Delta VTEC}{cos\phi} \quad \text{(Cycle)} \\ &= -\frac{1.687\times10^{-6}}{f} \cdot \frac{\Delta VTEC}{cos\phi} \quad \text{(Radian)} \end{aligned} \tag{10}$$

where $\Delta VTEC$ is the difference in VTEC between master and slave SAR images. Once $\Delta VTEC$ is determined, the ionospheric phase error φ_{ION} can be estimated from (10). However, as we mentioned in the introduction, there are the residual long-wavelength phase signals, if directly using the ionosphere-induced phase shift in (10) to correct the ionospheric effect on SAR interferometry. This problem has also been observed by Kim [44]. The residual long-wavelength signals can be attributed to the residual ionospheric phase noise according to their spatial characteristics. For the residual ionospheric phase, it may result from the inaccurate parameters, e.g., geomagnetic field parameters, system-dependent terms in FR estimation. To further improve the precision of ionospheric correction, an integrated phase model is used in this study, as follows:

$$\begin{aligned} \hat{\varphi}_{ION,ORB} = \quad & (\alpha_0 + \alpha_1 \cdot x + \alpha_2 \cdot y + \alpha_3 \cdot xy) \cdot \varphi_{ION} + \\ & (\beta_0 + \beta_1 \cdot x + \beta_2 \cdot y + \beta_3 \cdot xy + \beta_4 \cdot h(x,y)) \end{aligned} \tag{11}$$

where $\alpha_0, \alpha_1, \alpha_2$ and α_3 are the ionospheric model parameters, $\beta_0, \beta_1, \ldots, \beta_4$ are the residual ionospheric model parameters, x and y are the azimuth and range pixel location, and $h(x,y)$ is the topographic height at (x,y). $h(x,y)$ is involved in this process for mitigating the topography-dependent tropospheric phase error. It should be noted that the integrated phase model in (11) can only mitigate the stratified tropospheric delay, but can't mitigate the turbulent tropospheric delay. For retrieving model parameters in (11), least square estimation is used:

$$\begin{aligned} \varphi_{UNW} &= C \cdot \begin{bmatrix} \alpha \\ \beta \end{bmatrix} \\ min &= \left(C \cdot \begin{bmatrix} \alpha \\ \beta \end{bmatrix} - \varphi_{UNW} \right)^T \cdot \left(C \cdot \begin{bmatrix} \alpha \\ \beta \end{bmatrix} - \varphi_{UNW} \right) \\ Cond(\mathrm{C}) &= \| C \| \cdot \| C^{-1} \| \end{aligned} \tag{12}$$

where φ_{UNW} is the observed unwrapped phase, C is the designed matrix related with the pixel location involved in the parameters estimation, $\begin{bmatrix} \alpha \\ \beta \end{bmatrix}$ is the parameters matrix, *min* means minimization, T means matrix transpose, *Cond* (C) means the condition number of matrix C, $\| C \|$ means the norm of matrix C, and C^{-1} means the inverse of matrix C. The model parameters $\begin{bmatrix} \alpha \\ \beta \end{bmatrix}$ in (11) can be easily estimated by (12). However, in order to obtain robust parameter solutions, high coherence points with high-quality phase observations are selected to be involved in the parameter's estimation. This operation may reduce the distortion caused by the decorrelation noise. Then, phase observations at the selected high coherence points are extracted to calculate the model parameters through (12). After that, for further improvement of the stability of the solution, phase observations whose residual errors are above three times the root mean square error are excluded from the parameter's estimation. This process may reduce the distortions caused by other errors, such as stratified atmospheric delay. Finally, the updated phase observations are used to determine the model parameters. Once the model parameters in (12) are calculated, ionospheric phase errors are removed from the original interferograms.

3. Experiment and Analysis

For the performance test of the proposed method, L-band Advanced Land Observation Satellite (ALOS) Phase Array L-band SAR (PALSAR) full-polarimetric SAR images over high-latitude and

low-latitude regions are processed. Table 1 lists the interferometric parameters for the collected SAR images over the experimental regions.

Table 1. Interferometric parameters used in the experiment, where B_T stands for temporal baseline and B_P stands for perpendicular baseline.

No.	Master	Slave	Center Frequency	Incident Angle	Center Latitude	Center Longitude	B_T (Days)	B_P (m)
1	01/04/2007	17/05/2007	1270 MHz	23.93°	62.47°	−144.77°	46	6
2	26/03/2010	29/03/2011	1270 MHz	24.01°	100.56°	14.87°	368	1091

3.1. Case 1: High-Latitude Region

3.1.1. Experimental Region and Data

The experimental region with high latitude is located in Alaska, which is the largest state in the United States by area and situated in the northwest extremity of the Americas (Figure 2a). Two L-band full-polarimetric ALOS/PALSAR images acquired on 1 April 2007 and 17 May 2007 were collected in this experiment. As shown in Table 1, the temporal baseline is 46 days and perpendicular baseline is 6 m.

For generating reference information about ionospheric variation at the SAR acquisition time, the dual-frequency GPS data at a permanent station near Fairbanks is processed (the red star in Figure 2a). This procedure is carried out by calculating the GPS carrier phase difference between frequency L1 and L2. This difference can remove the tropospheric delays errors and GPS receiver clock errors because they have the same effects on the observation for both frequency L1 and L2 [16]. Moreover, the inter-frequency difference in satellite clock offsets are so small that they can be neglected. As for the receiver and satellite's instrumental biases, they can be cancelled since they remain constant over a short observation session. Finally, the cycle slips are detected and corrected using the algorithm proposed by Blewitt [49]. After these operations, the residual phase components are mainly from the ionospheric contribution. Figure 2b,c shows the time rate of changes of total electronic content (ROT), an index to reflect the ionospheric variation) on 1 April 2007 and 17 May 2007, respectively, where SAR acquisition time is marked with a dotted line. Figure 2b presents the clear ionospheric fluctuation from 5:00 to 18:00 UT and a peak value at about 7:00 UT. This suggests the strong ionospheric irregularities over experimental area on 1 April 2007. Unlike Figure 2b,c shows the weak ionospheric irregularities, indicating the background ionospheric condition on 17 May 2007. Additionally, the Auroral Electrojet (AE) index, a quantitative measure of auroral zone magnetic activity, was obtained from the Super Dual Auroral Radar Network (SuperDARN) (http://vt.superdarn.org/tiki-index.php?), as shown in Figure 2d–e. It is found that the geomagnetic activity is relatively strong on 1 April, when the AE value at the SAR-acquired time is about 600 nT. The geomagnetic activity is quiet on 17 May, when the AE value at the SAR-acquired time is about 80 nT. This result provides another piece of evidence for ionospheric irregularities on 1 April 2007 and the background ionospheric condition on 17 May 2007.

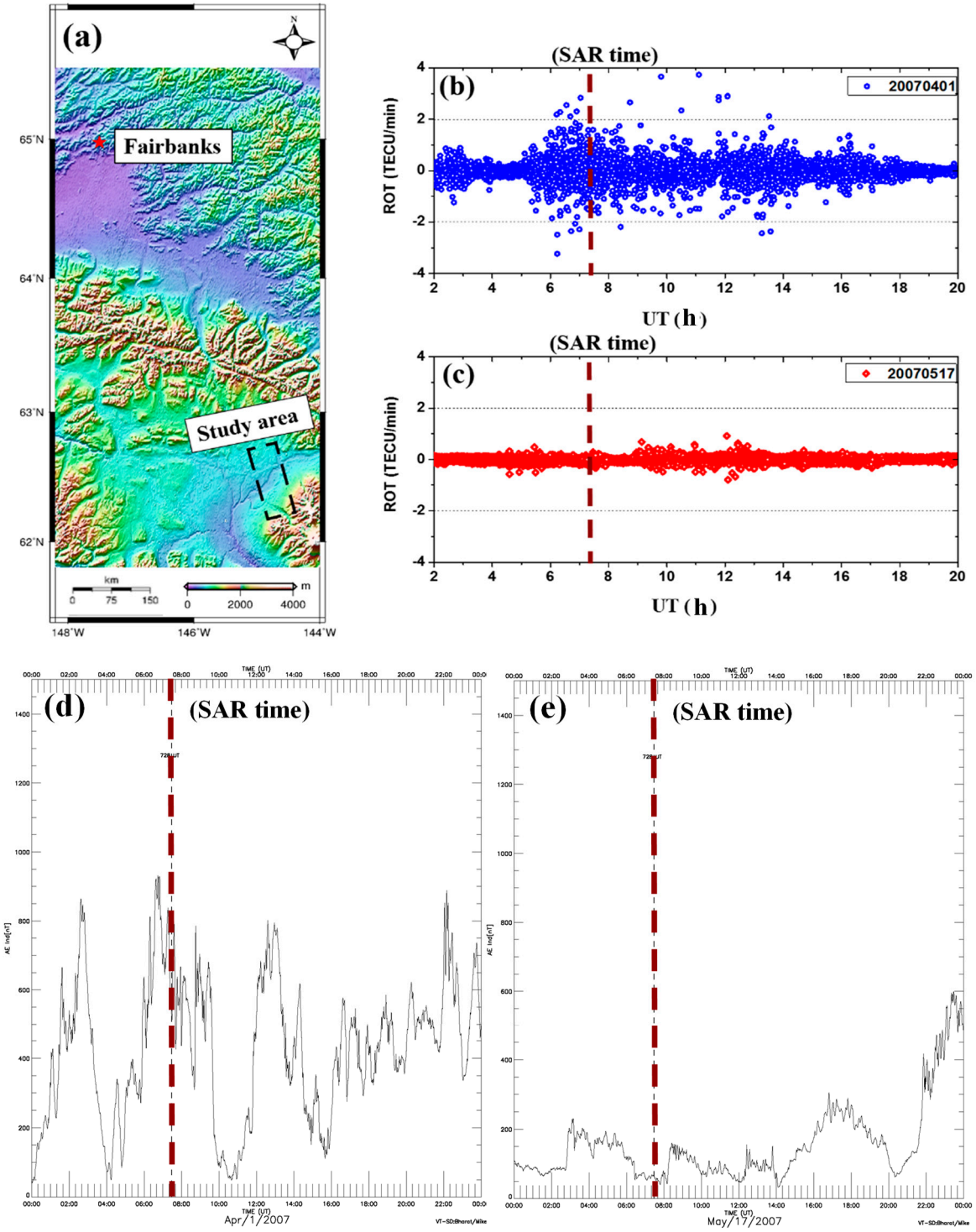

Figure 2. Experimental region and Global Positioning System (GPS)-measured ionospheric variations at Synthetic aperture radar (SAR) acquisition time. (**a**) Experimental area. The black rectangle denotes the spatial coverage of SAR images and red pentagram shows the location of a dual-frequency GPS station, (**b**,**c**) GPS-measured the time rate of changes of total electronic content(ROT) values on 1 April and 17 May 2007, respectively, (**d**,**e**) AE variations on April and May 2007, respectively.

3.1.2. FR and VTEC Estimations

For the collected SAR data with raw format (L0 level), they have to be processed to the single look complex (SLC) format (L1 level). During this procedure, the system-dependent terms of A, $e^{j\Phi}$, R, and

T in (1) are calibrated [50]. Then, measured scattering matrices M are formed from the full-polarimetric SLC data. The linear polarization scattering matrix M is transformed into circular polarized scattering matrix Z based on (4) and complex matrices of $Z_{LR} \times Z_{RL}^{*}$ are created. For suppressing the noises and preserving the same ground resolution in both of range and azimuth directions, multi-looking operation of complex image with two looks in the range direction and 14 looks in the azimuth direction is applied to the $Z_{LR} \times Z_{RL}^{*}$. To reduce phase noise, the Goldstein adaptive filter with a window size of 32 is applied to the multi-looked data [51]. Finally, FR angles from two images are produced by (7), as shown in Figure 3.

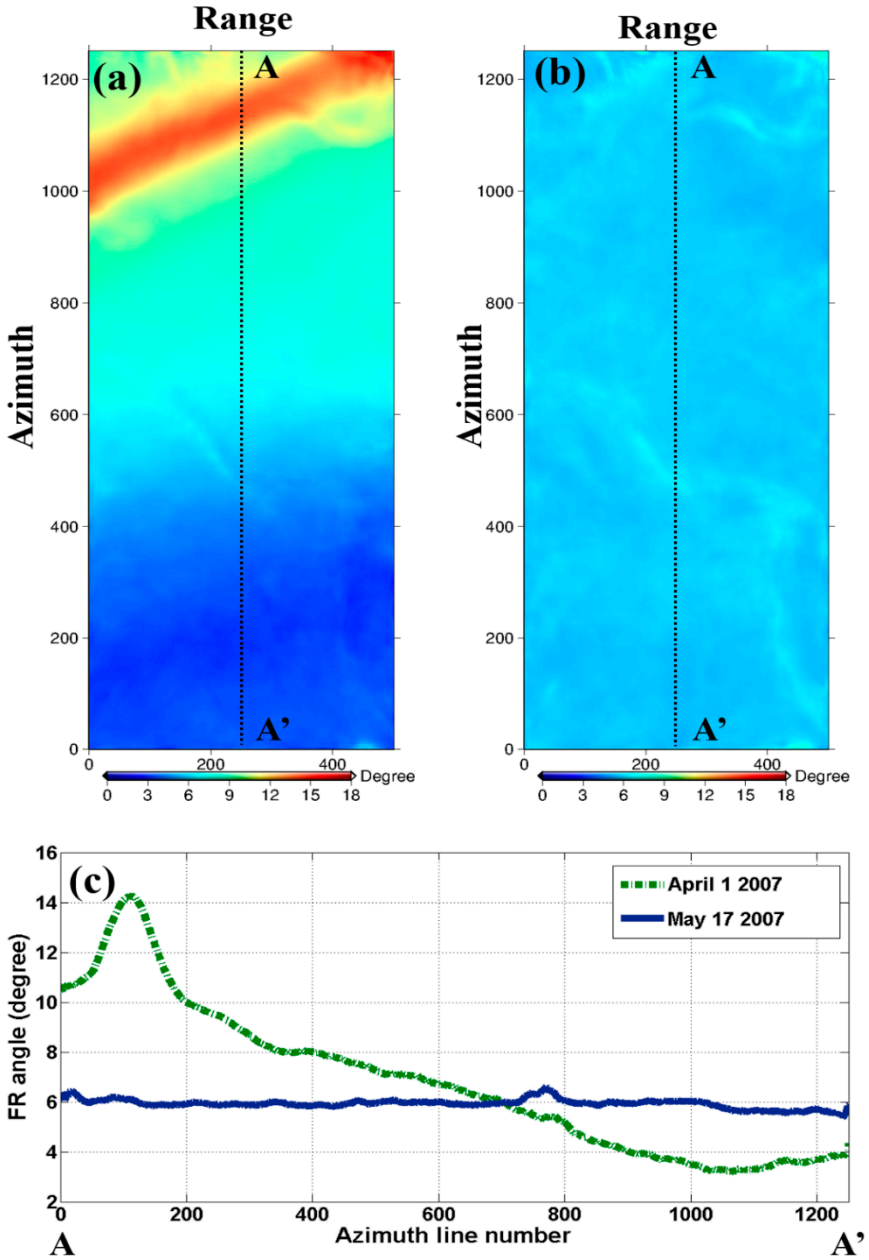

Figure 3. Faraday rotation (FR) angles. (**a**,**b**) FR angle maps from 1 April and 17 May 2007, respectively, (**c**) the FR angle values in the profiles A-A′ of (**a**) and (**b**).

Figure 3a,b represents the spatial distributions of FR on 1 April 2007 and 17 May 2007, respectively. Figure 3a shows that prominent inhomogeneity of FR distribution appears in the whole image, particularly for the upper part of image, where a maximum value of 16.9° is observed. The mean

value and standard deviation of FR angles are respectively 6.8° and 2.9° in Figure 3a. Compared to Figure 3a, Figure 3b shows spatially homogenous FR angles. The standard deviation of FR angles in Figure 3b is 0.18°. Figure 3c depicts the FR differences between profiles A-A' of Figure 3a,b. It can be observed from Figure 3c that a gradient is recorded for FR angles on 1 April 2007. Because the system-dependent terms and noise have been calibrated and mitigated, the estimated FR angles in Figure 3a,b are considered to be primarily introduced by the ionosphere. For Figure 3a, it can be assumed that there are the ionospheric irregularities, which results in the FR angle inhomogeneity and SAR image distortion. However, for Figure 3b, there is the weak ionospheric irregularities. On the other hand, it is also observed from Figure 3a,b that there is a certain FR estimation error, particularly for Figure 3b. According to FR estimation theory, this error may be caused by the calibration parameters, such as channel imbalance f_1 and f_2, crosstalk terms δ_1, δ_2, δ_3 and δ_4, additional noise N, as well as backscatter characteristics of the imaged surface.

Once FR angles are determined, the vertical total electronic content (VTEC) distribution can be generated from (9). For this process, the geomagnetic field parameters are required. The eleventh generation International Geomagnetic Reference Field (IGRF), which is a standard mathematical description of the Earth's main magnetic field [52], was used for this case. Using SAR acquisition time and area, the geomagnetic field parameters are extracted from the IGRF and projected to the SAR coordinate system. Then, the geomagnetic field factor $\overline{B \cdot cos\theta \cdot sec\phi}$ at a constant height of 400 km was determined using geomagnetic field and SAR imaging geometry. Figure 4a shows the geomagnetic intensity at a 400 km height on 1 April 2007, which varies from 0.466 to 0.478 Gauss (1Gauss = 10^5 nT).

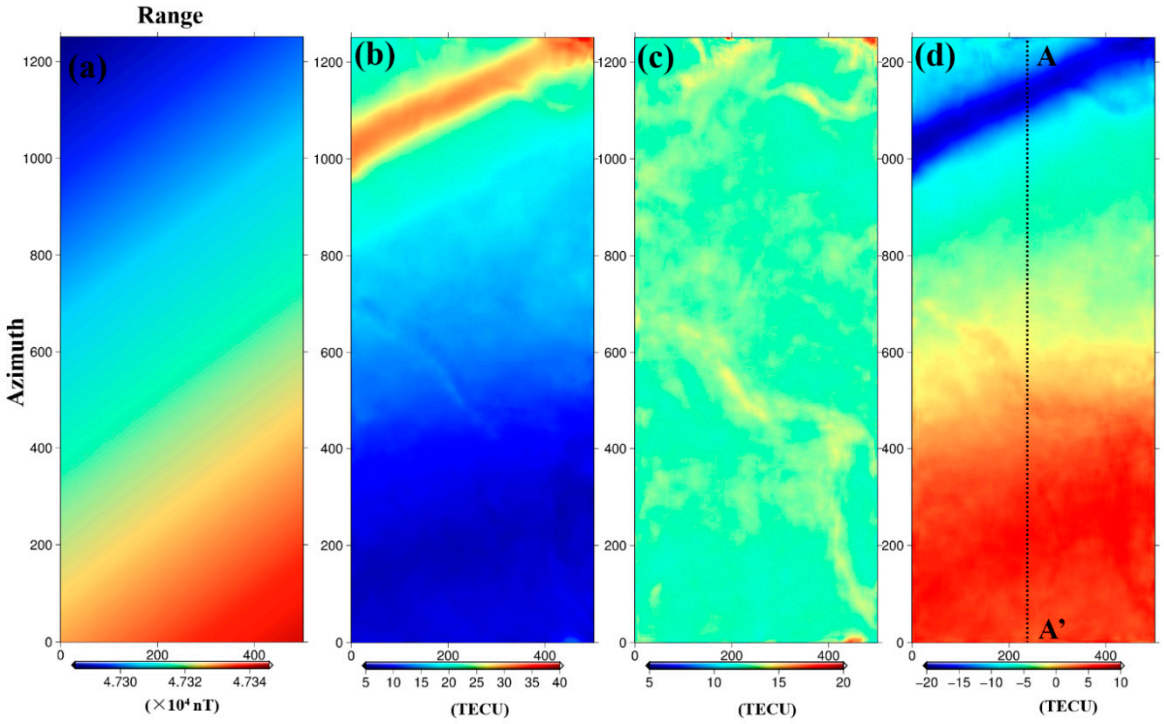

Figure 4. Vertical total electronic content (VTEC) maps inverted from FR angles. (**a**) *B* value of the geomagnetic field on 1 April 2007; (**b**,**c**) VTEC maps on 1 April and 17 May 2007, respectively, (**d**) the difference between (**b**) and (**c**).

Figure 4b,c presents the spatial distributions of VTEC on 1 April 2007 and 17 May 2007, respectively. It is observed that both Figures 3a and 4b show the stripe-shaped ionospheric anomaly in the upper part of images and prominent inhomogeneity across the whole image, whereas Figures 3b and 4c maintain uniformity across the whole image. This result is consistent with GPS-measured ionospheric variation in Figure 2b,c. The maximum magnitudes of Figure 4b,c are 35.9 and 17.8 Total electron

content unit (TECU), respectively. Furthermore, the mean and standard deviations are 14.1 and 6.2 TECU for the VTEC map of Figure 4b, respectively, and 12.2 and 0.37 TECU for the VTEC map of Figure 4c, respectively. The small difference in mean value suggests that the background ionospheric condition is similar at both SAR acquisition times. Figure 4d shows the VTEC differences between two SAR acquisitions. The VTEC differences produce additional ionospheric phase errors on the interferogram. Figure 5 presents the VTEC differences in profile A-A' of Figure 4d, which indicates that the ionospheric disturbance on the interferogram may be severe.

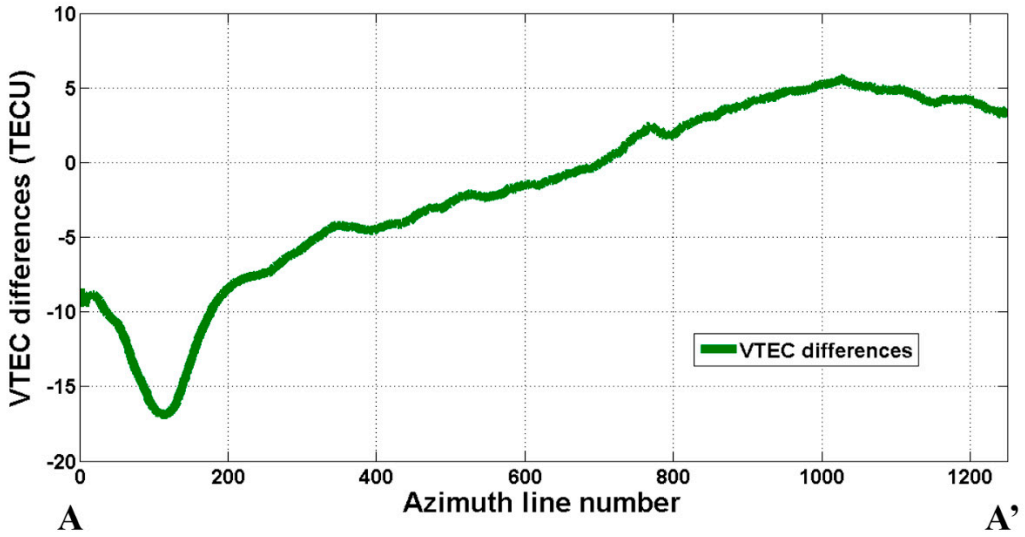

Figure 5. VTEC difference map in profile A-A' of Figure 4d.

3.1.3. Mitigation of Ionospheric Effects on SAR Interferometry

The SAR interferogram was generated from two L-band full-polarimetric ALOS/PALSAR raw data, which were acquired on 1 April 2007 and 17 May 2007. The ASTER Global Digital Elevation Model (GDEM) with a resolution of 1 arc-seconds (30 m) was used to remove the topographic phase (Figure 6). A complex multi-look operation of two looks in the range direction and 14 looks in the azimuth direction, and an adaptive spectral filtering with a window size of 32 were applied to reduce the interferometric phase noise. Moreover, the interferogram was unwrapped by the minimum cost flow (MCF) method [53].

Figure 7 shows the Horizontal-Horizontal (HH)-polarized original and corrected interferogram. Figure 7a represents the original interferogram, where the complicated phase patterns are observed. The main contributions of these patterns might result from the ionospheric errors based on the presented observation conditions. Figure 7b derived from (10) demonstrates the severe ionospheric effects. These effects range from −23.2 to 47.5 rad., which correspond to line-of-sight (LOS) displacements of −0.43 to 0.89 m. This error can severely degrade the precision of surface deformation monitoring or DEM construction when using the InSAR technique. Figure 7c conveys the interferogram generated by subtracting the ionospheric phase map (Figure 7b) from the original interferogram (Figure 7a). As observed in Figure 7c, most long-wavelength signals in the original interferogram have been successfully removed. This fact indicates that the estimated ionospheric phase successfully mitigates the ionospheric phase distortion. However, the residual long-wavelength signal still remains, which can be attributed to the residual ionospheric phase error. The residual ionospheric phase results from the inaccurate parameters, such as the magnetic field factor and some systematic bias. Figure 7d shows the residual-ionosphere-corrected interferogram, which is generated by subtracting the fitted residual ionospheric phase in (11). However, as observed in Figure 7d, considerable amounts of ionospheric phase error remain, particularly at the top and bottom parts of the interferogram. Finally, Figure 7e shows the interferogram that is jointly corrected by the least square method from (11). The estimated

model parameter is shown in Table 2. It can be clearly seen that the complicated fringes in original interferogram have been removed. The remaining major error components of Figure 7e may be attributed to the turbulent tropospheric delay.

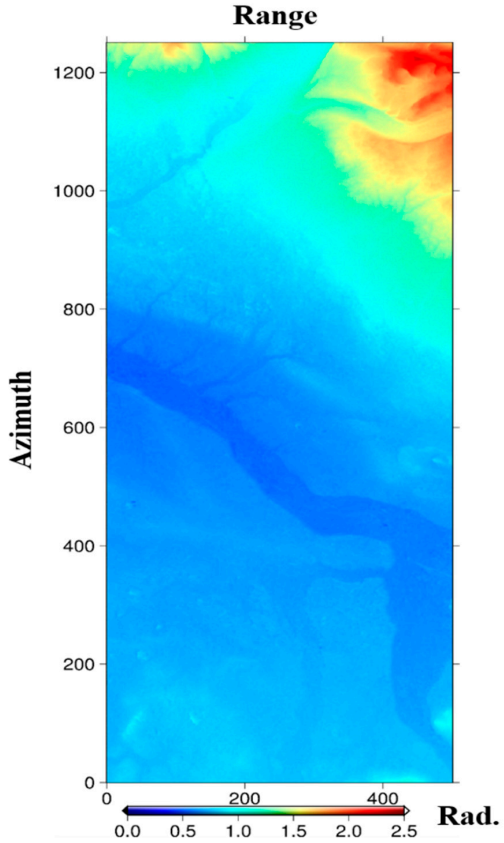

Figure 6. Simulated topographic phase used in this experiment.

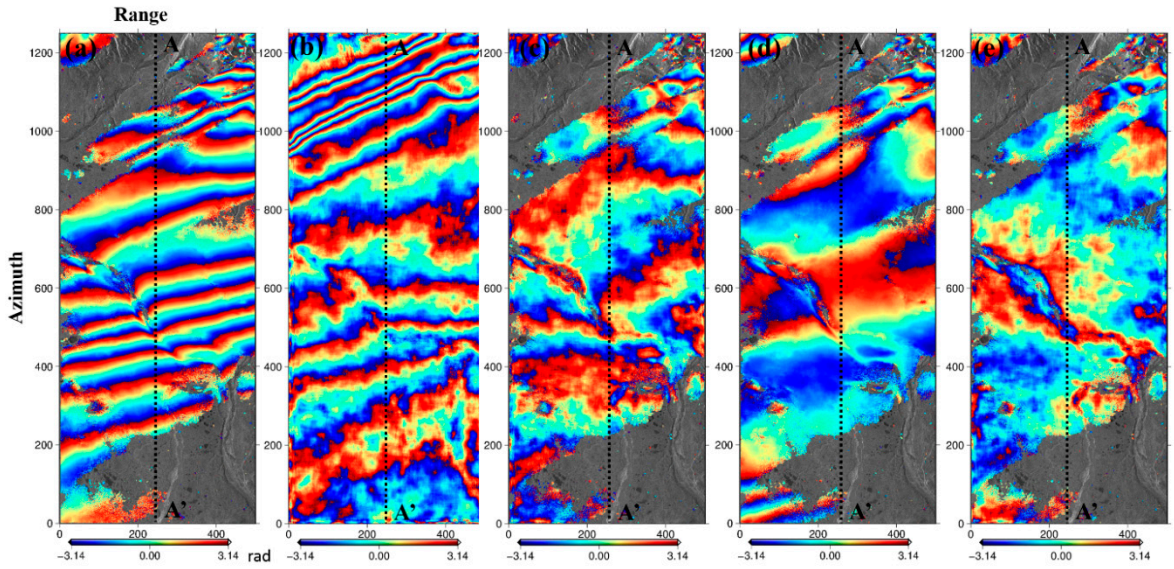

Figure 7. Horizontal- Horizontal (HH)-polarized original and corrected interferogram. (**a**) Original interferogram, (**b**) ionospheric phase map derived from (10), (**c**) ionosphere-corrected interferogram by subtracting Figure 7b from Figure 7a, (**d**) residual-ionosphere-corrected interferogram by subtracting the fitted residual ionospheric phase from Figure 7a, (**e**) integration-corrected interferogram by subtracting the fitted phase in (11) from Figure 7a.

Table 2. Estimated model parameters used to remove the ionsopheric errors.

α_0	α_1	α_2	α_3	β_0	β_1	β_2	β_3	β_4
−1.625	−0.0026	−0.0055	9.321×10^{-6}	−15.504	−0.016	−0.0125	4.49×10^{-8}	7.97×10^{-4}

3.1.4. Validation of Ionospheric Correction

Figure 8 presents the interferometric phase at the profile A-A′ in Figure 7a,c–e. It is found that the integration-corrected interferometric phase becomes more stable, implying that the proposed method can effectively mitigate ionospheric errors. For the whole images, the statistics show that the mean standard deviations have reduced nearly a factor of eight times for corrected phase (2.5 rad) versus original phase (21.6 rad), demonstrating the validation of our correction once more.

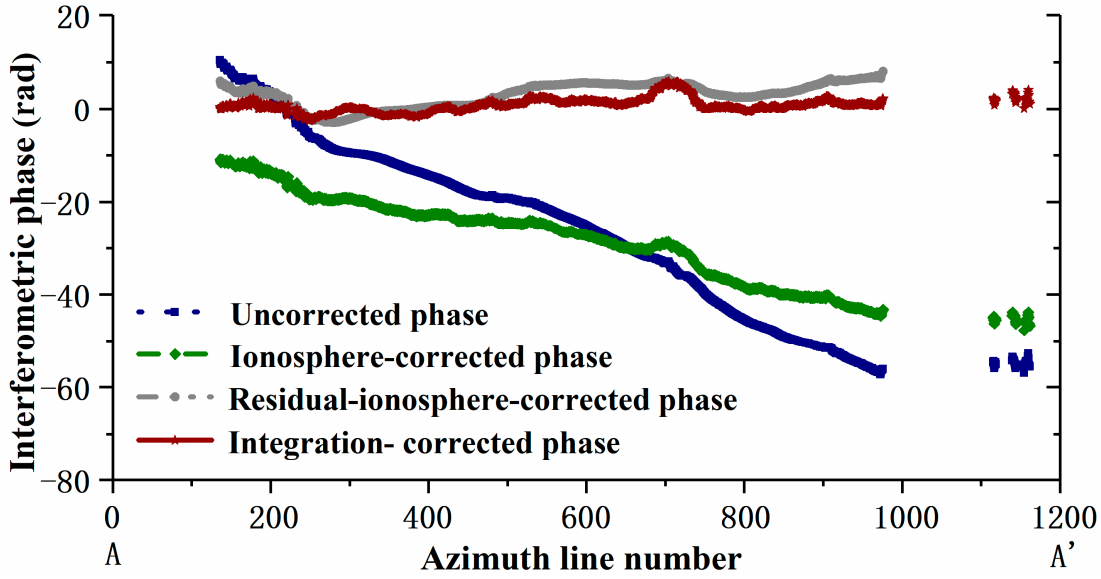

Figure 8. Comparison among the interferometric phase in the profile A-A′ in Figure 7a,c,d.

3.2. Case 2: Low-Latitude Region

3.2.1. Experimental Region and Data

The experimental region with low latitude is located in Thailand, which is a country at the center of the Southeast Asian Indochinese peninsula (Figure 9a). Two L-band full-polarimetric ALOS/PALSAR images acquired on 23 March 2010 and 29 March 2011 were collected in this region (Table 1). As Thailand is located at a latitude of 15° N, which is directly under the north equatorial ionospheric anomaly region, the phenomenon of ionospheric irregularities often occurs in this area. Figure 9b,c show the International Global Navigation Satellite System (GNSS)Service (IGS) global vertical total electron content (VTEC) maps at 16:00 (UT) on 23 March 2010 and 29 March 2011 (3 min after the SAR time), respectively. It is clearly observed that the collected SAR images (black rectangle) lie in this ionospheric anomaly region at the SAR-acquired time. Thus, it is predicted that the generated interferogram from these two images will be contaminated by the ionosphere.

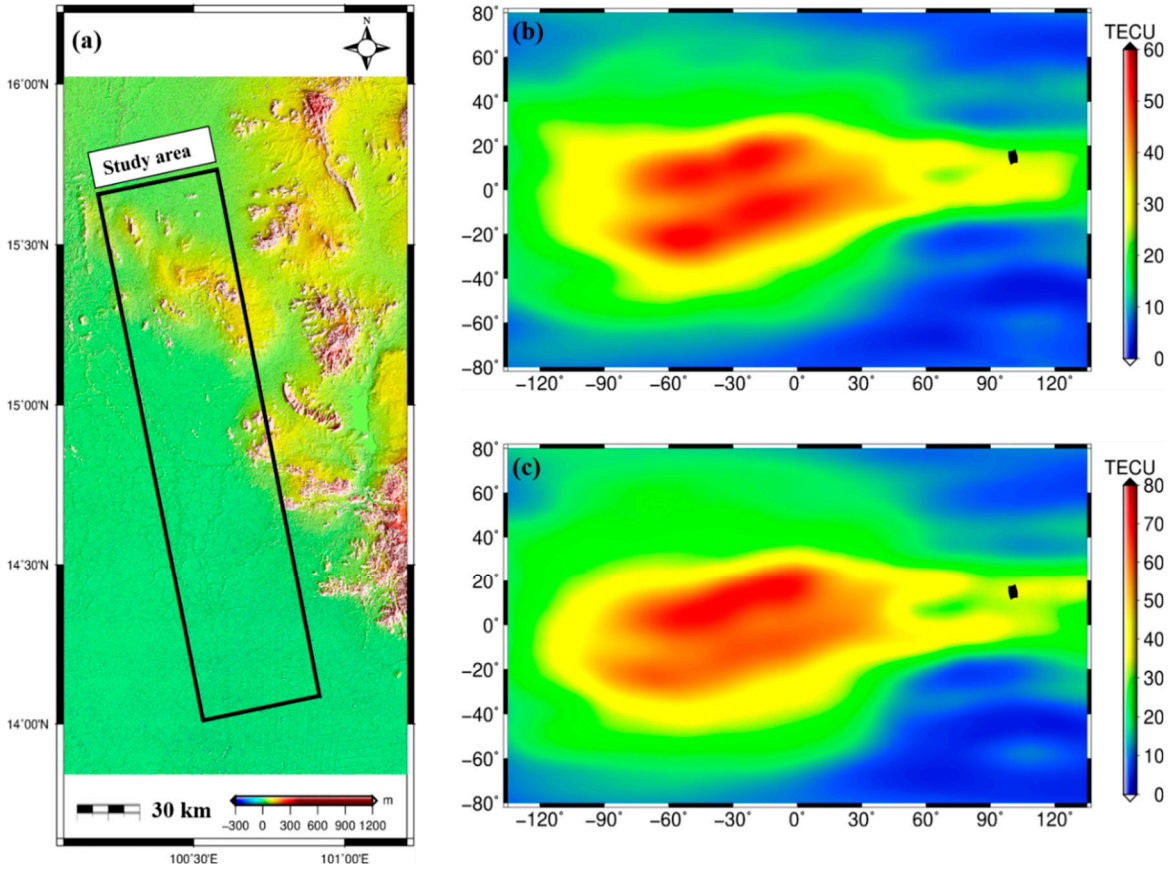

Figure 9. Experimental region and the International Global Navigation Satellite System (GNSS) Service (IGS) VTEC maps. (**a**) Experimental area; (**b**,**c**) IGS VTEC maps at 16:00 (UT) on 26 March 2010 and 29 March 2011, respectively. The black rectangle denotes the spatial coverage of SAR images.

3.2.2. FR and VTEC Estimations

The FR and VTEC maps are estimated over Thailand with the same procedure that was used for Alaska. Figure 10a,b represents the spatial distributions of FR on 26 March 2010 and 29 March 2011, respectively. It is found that both maps show the spatially homogenous FR angles, where the standard deviations are 0.23° and 0.20° on 26 March 2010 and 29 March 2011, respectively. This observation is different from the last experiment, where the prominent stripe-shaped FR distribution is found. However, careful inspection suggests that there is a clear difference in FR magnitude between Figure 10a,b: Figure 10b illustrates larger FR values than Figure 10a. Because the system-dependent terms and noise have been calibrated and mitigated, this difference is considered to be primarily introduced by the ionosphere. Figure 10c,d displays the spatial distributions of VTEC on 26 March 2010 and 29 March 2011, respectively. It is observed that both Figure 10c,d show a similar pattern with Figure 10a,b. The maximum magnitudes of Figure 10c,d are 31 and 45 TECU, respectively. The mean values are 25 TECU for Figure 10c and 41 TECU for Figure 10d, showing the comparable results with Figure 9b,c. Due to the different VTEC magnitude, the additional ionospheric phase error may be produced when the interferogram is formed from these collected SAR images.

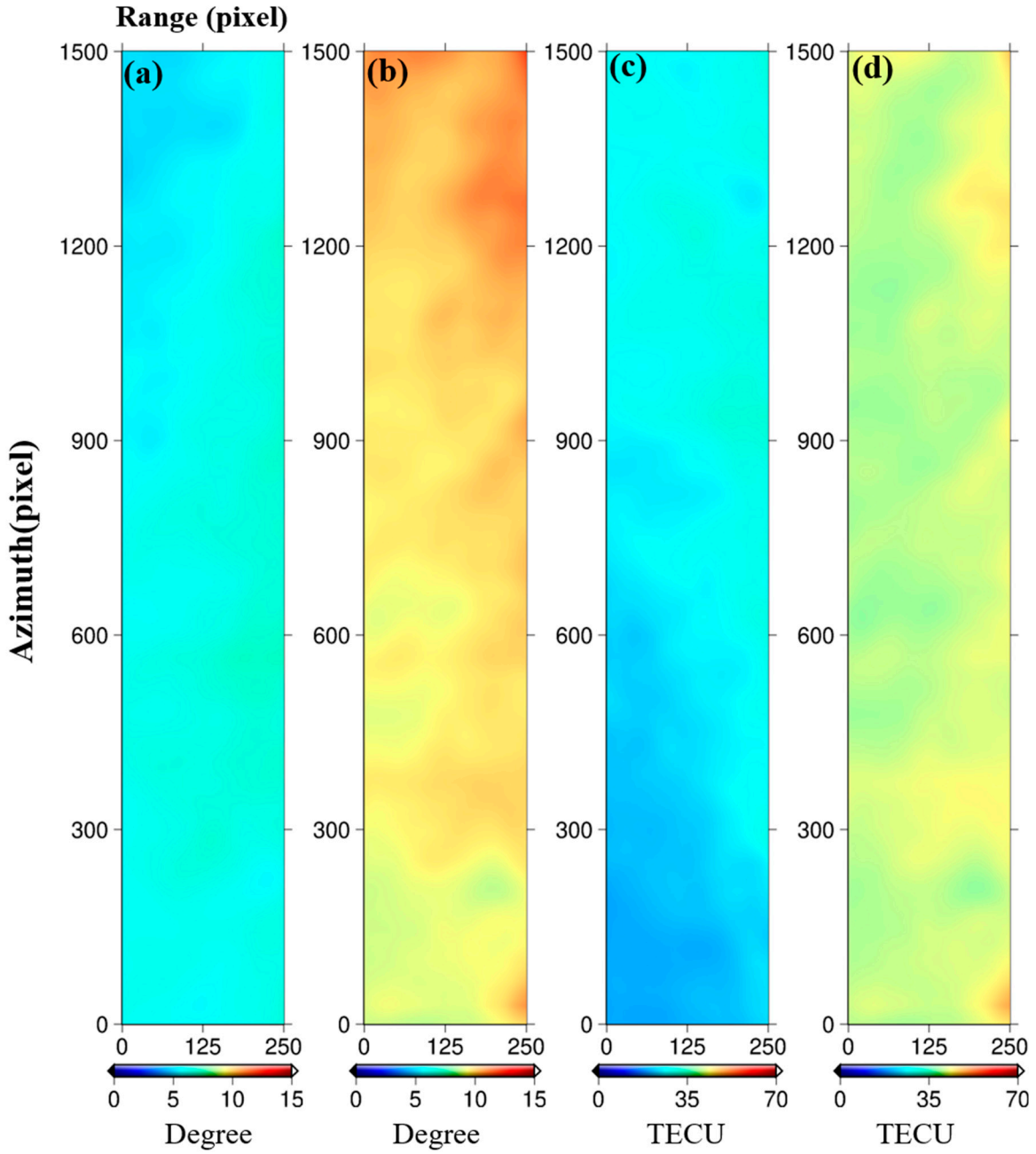

Figure 10. FR angles and VTEC maps. (**a**,**b**) FR angles on 26 March 2010 and 29 March 2011, respectively; (**c**,**d**) VTEC maps on 26 March 2010 and 29 March 2011, respectively.

3.2.3. Mitigation of Ionospheric Effects on SAR Interferometry

To mitigate the ionospheric effect, the proposed method is applied to the data from Thailand. Figure 11 shows the HH-polarized original and corrected interferogram. Figure 11a, displaying the original interferogram, indicates that main phase contribution is from the ionospheric error based on the presented long-wavelength characteristics. Figure 11b shows the residual-ionosphere-corrected interferogram, which is generated by subtracting the fitted residual ionospheric phase in (11) from Figure 11a. It is found that most long-wavelength signals have been successfully removed. However, the residual long-wavelength signal still remains, which can be attributed to the ionospheric phase error. Figure 11c conveys the interferogram generated by subtracting the ionospheric phase map from the original interferogram. As observed in Figure 11c, most of the long-wavelength signal remains, which is mainly from the residual ionospheric phase error. Figure 11d shows the interferogram that

is jointly corrected by the least square method from (11). It can be clearly seen that almost all the long-wavelength signals have been successfully removed from Figure 11a, demonstrating the reliability of the proposed method. The residual phase in Figure 11d may be from the turbulent tropospheric phase delay and topographic phase error.

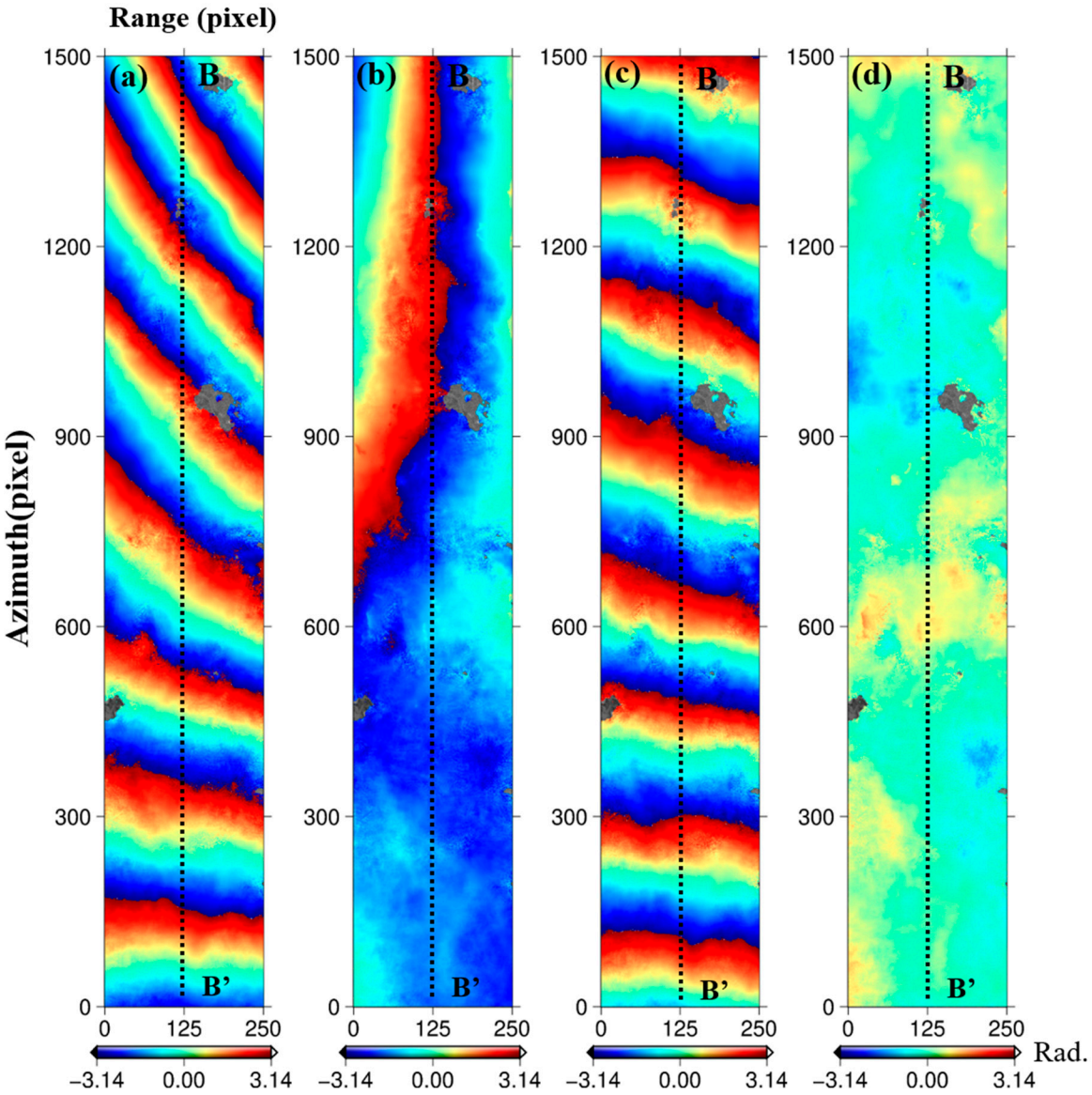

Figure 11. HH-polarized original and corrected interferogram. (**a**) Original interferogram, (**b**) residual-ionosphere-corrected interferogram by subtracting the fitted residual ionospheric phase from Figure 11a, (**c**) ionosphere-corrected interferogram by subtracting ionospheric phase from Figure 11a, (**d**) integration-corrected interferogram by subtracting the fitted phase in (11) from Figure 11a.

3.2.4. Validation of Ionospheric Correction

Figure 12 presents the interferometric phase at the profile B-B′ in Figure 11a,c,d. It is observed that the integration-corrected interferometric phase is close to zero, while the other two show the obvious phase error. The statistics shows that the standard deviations have reduced nearly a factor of 28 times for integration-corrected phase (0.46 rad) versus original phase (12.83 rad) in this case. Both results demonstrate the validation of our correction.

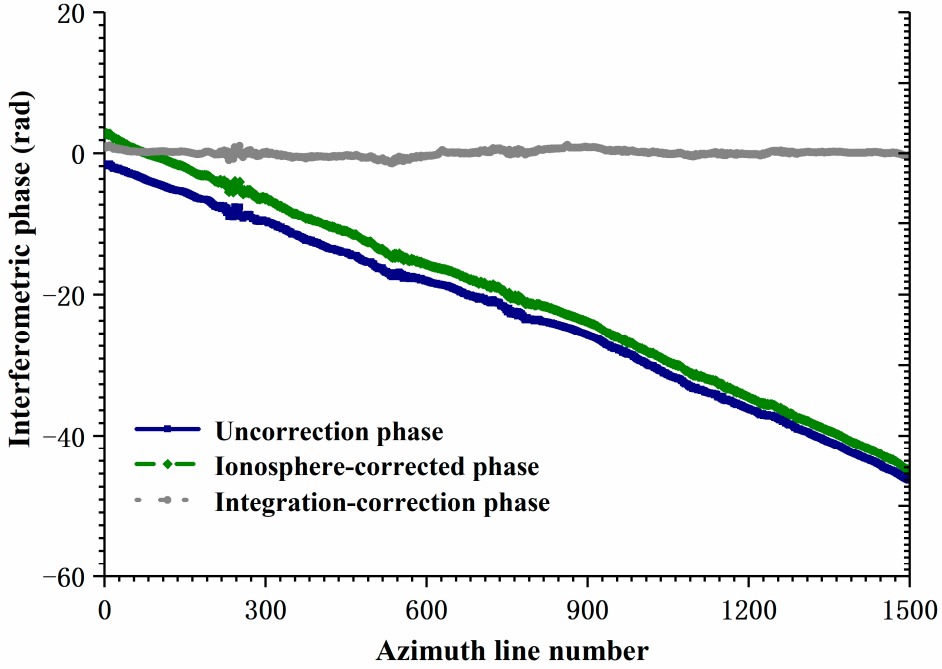

Figure 12. Comparison among the interferometric phase in the profile B-B′ in Figure 11a,c,d.

4. Conclusions

With the increasing interest in the use of low-frequency SAR systems, such as L- and P-bands, the influence on SAR interferometry due to the ionosphere continues to become significant and therefore limits further development of the InSAR technique. In this situation, this paper presents an efficient FR-based method to mitigate the ionospheric phase errors on polarimetric SAR interferograms. Compared with the existing methods, the proposed method uses an integrated phase model, which can correct the ionospheric errors as well as residual ionospheric phase errors caused by inaccurate parameters on SAR interferometry, and thus improve the correction precision. For the performance test, L-band ALOS/PALSAR full-polarimetric SAR images over high-latitude and low-latitude regions are processed. Based on this study, the following conclusions are summarized:

(1) Ionospheric phase error on full-polarimetric SAR interferometry is effectively mitigated by the proposed FR-based method. Using inversed VTEC distribution from FR angles, an integrated phase model is used to jointly mitigate the ionospheric phase errors. The experimental results show that most ionospheric phase errors are removed from the original phase. These results validate that the FR-based method can effectively mitigate the ionospheric phase errors.

(2) The VTEC distribution with high spatial resolution is successfully mapped from the full-polarimetric SAR data. In this study, the high-spatial-resolution VTEC distribution is inversed from FR angles. When comparing with the GPS-measured ionospheric variations, we found that they are basically consistent. These results prove that it is possible to map the high-spatial-resolution VTEC distribution from the full-polarimetric SAR data.

Although the reliability of the FR-based method has been proven by two experiments, there are still some limitations. The first is the FR estimation error due to the inaccurate calibration parameters, such as channel imbalance $f1$ and $f2$, crosstalk terms $\delta 1$, $\delta 2$, $\delta 3$ and $\delta 4$, additional noise N, as well as backscatter characteristics of the imaged surface. Since the ionosphere-induced phase shift in (10) is derived from the estimated FR, this error will inevitably introduce bias in the ionospheric correction when using (11). Another limitation is the imprecise geomagnetic field parameters, such as the intensity of earth's magnetic field. In this study, the geomagnetic field parameters are derived from the IGRF, which is a standard mathematical description of the Earth's main magnetic field. In other words, it is difficult to obtain the actual local geomagnetic activity, resulting in the imprecise estimation of VTEC.

Although the proposed method can correct part of residual ionospheric phase error caused by the inaccurate calibration parameters and imprecise geomagnetic field parameters, it is difficult to remove them completely, particularly for the small-scale residual ionospheric phase. The final limitation is that some useful phase signals with long-wavelength characteristics may be removed when using our proposed method, such as interseismic deformation. Therefore, multi methods, such as range split-spectrum based method, range/azimuth offset based methods, as well as the FR based method, will be fused in the future to improve the precision of the ionospheric correction on SAR interferometry.

Author Contributions: Validation, J.-Y.C.; Writing—original draft, W.Z.; Writing—review & editing, H.-S.J.

Funding: This research was funded by Chang'an university (Xi'an, China) through National Key R&D Program of China (2018YFC1505101), Natural Science Foundation of China projects (NSFC) (No: 41790445, 41731066, 41504005, 41674001, 41604001), Natural Science Basic Research Plan in Shaanxi Province of China (2018JQ4031), and the Fundamental Research Funds for the Central Universities, CHD (No: 300102269207, 300102269303). This research was also funded by the Korea Meteorological Administration Research and Development Program under Grant KMIPA2015-3071.

Acknowledgments: Several figures were prepared by using Generic Mapping Tools software. We are grateful to the anonymous reviewers for their constructive comments to improve this manuscript.

Conflicts of Interest: The authors declare no conflict of interest.

References

1. Rosen, P.A.; Hensley, S.; Zebker, H.A.; Webb, F.H.; Fielding, E.J. Surface deformation and coherence measurements of Kilauea Volcano, Hawaii, from SIR-C radar interferometry. *J. Geophys. Res.* **1996**, *101*, 23109–23125. [CrossRef]
2. Zhu, W.; Zhang, Q.; Ding, X.L.; Zhao, C.Y.; Yang, C.S.; Qu, W. Recent ground deformation of Taiyuan basin (China) investigated with C-, L-, and X-bands SAR images. *J. Geodyn.* **2013**, *70*, 28–35. [CrossRef]
3. Buhari, M.D.; Tian, G.Y.; Tiwari, R.; Muqaibel, A.H. Multicarrier SAR Image Reconstruction Using Integrated MUSIC-LSE Algorithm. *IEEE Access* **2018**, *6*, 22827–22838. [CrossRef]
4. Zhang, Y.; Guan, T.; Duan, L.; Wei, B.; Gao, J.; Mao, T. Inertial sensors supported visual descriptors encoding and geometric verification for mobile visual location recognition applications. *Signal Process.* **2015**, *112*, 17–26. [CrossRef]
5. Brcic, R.; Parizzi, A.; Eineder, M.; Bamler, R.; Meyer, F. Estimation and Compensation of Ionospheric Delay for SAR Interferometry. In Proceedings of the 2010 IEEE International Geoscience and Remote Sensing Symposium (IGARSS), Honolulu, HI, USA, 25–30 July 2010; pp. 2908–2911.
6. Brcic, R.; Parizzi, A.; Eineder, M. Ionospheric effects in SAR interferometry: An analysis and comparison of methods for their estimation. In Proceedings of the 2011 IEEE International Geoscience and Remote Sensing Symposium (IGARSS), Vancouver, BC, Canada, 24–29 July 2011; pp. 1497–1500.
7. Hanssen, R. *Radar Interferometry: Data Interpretation and Error Analysis*; Kluwer Academic: Dordrecht, The Netherlands; Boston, MA, USA, 2001.
8. Pi, X.; Freeman, A.; Chapman, B.; Rosen, P.; Li, Z.H. Imaging ionospheric inhomogeneities using spaceborne synthetic aperture radar. *J. Geophys. Res.* **2011**, *116*, A04303. [CrossRef]
9. Bickel, S.H.; Bates, R.H.T. Effects of Magneto-Ionic Propagation on the Polarization Scattering Matrix. *Proc. IEEE.* **1965**, *53*, 1089–1091. [CrossRef]
10. Rignot, E.J.M. Effect of Faraday rotation on L-band interferometric and polarimetric synthetic-aperture radar data. *IEEE Trans. Geosci. Remote Sens.* **2000**, *38*, 383–390. [CrossRef]
11. Wright, P.A.; Quegan, S.; Wheadon, N.S.; Hall, C.D. Faraday rotation effects on L-band spaceborne data. *IEEE Trans. Geosci. Remote Sens.* **2003**, *41*, 2735–2744. [CrossRef]
12. Freeman, A.; Saatchi, S. On the Detection of Faraday Rotation in Linearly Polarized L-Band SAR Backscatter Signatures. *IEEE Trans Geosci Remote Sens.* **2004**, *42*, 1607–1616. [CrossRef]
13. Meyer, F.; Nicoll, J. Prediction, detection, and correction of Faraday rotation in full-polarimetric L-band SAR data. *IEEE Trans. Geosci. Remote Sens.* **2008**, *46*, 3076–3086. [CrossRef]
14. Gray, A.L.; Mattar, K.E.; Sofko, G. Influence of ionospheric electron density fluctuations on satellite radar interferometry. *Geophys. Res. Lett.* **2000**, *27*, 1451–1454. [CrossRef]

15. Wegmuller, U.; Werner, C.; Strozzi, T.; Wiesmann, A. Ionospheric electron concentration effects on SAR and InSAR. In Proceedings of the 2006 IEEE International Symposium on Geoscience and Remote Sensing (IGARSS), Denver, CO, USA, 31 July–4 August 2006; pp. 3731–3734.
16. Zhu, W.; Ding, X.L.; Jung, H.S.; Zhang, Q.; Zhang, B.C.; Qu, W. Investigation of ionospheric effects on SAR Interferometry (InSAR): A case study of Hong Kong. *Adv. Space Res.* **2016**, *58*, 564–576. [CrossRef]
17. Liu, J.; Kuga, Y.; Ishimaru, A. Simulations of ionospheric effects on SAR at P-band. In Proceedings of the 1999 International Geoscience and Remote Sensing Symposium (IGARSS), Hamburg, Germany, 28 June–2 July 1999; pp. 1842–1844.
18. Liu, J.; Kuga, Y.; Ishimaru, A. Ionosheric effect on SAR imaging: A numerical study. *IEEE Trans. Geosci. Remote Sens.* **2003**, *41*, 939–947.
19. Davies, K.; Smith, E.K. Ionospheric effects on satellite land mobile systems. *IEEE Antennas Propag. Mag.* **2002**, *44*, 24–31. [CrossRef]
20. Meyer, F.; Bamler, R.; Jakowski, N.; Fritz, T. The potential of low frequency SAR systems for mapping ionospheric TEC distributions. *IEEE Trans. Geosci. Remote Sens. Lett.* **2006**, *3*, 560–564. [CrossRef]
21. Meyer, F. A review of ionospheric effects in low-frequency SAR-signals, correction methods, and performance requirements. In Proceedings of the 2010 IEEE International Geoscience and Remote Sensing Symposium (IGARSS), Honolulu, HI, USA, 25–30 July 2010; pp. 29–32.
22. Meyer, F. Performance requirements for ionospheric correlation of low-frequency SAR data. *IEEE Trans. Geosci. Remote Sens.* **2011**, *49*, 3695–3702. [CrossRef]
23. Chapin, E.; Chan, S.F.; Chapman, B.D. Impact of the ionosphere on an L-band space based radar. In Proceedings of the 2006 IEEE Conference on Radar, Verona, NY, USA, 24–27 April 2006; pp. 51–58.
24. Rosen, P.A.; Hensley, S.; Chen, C. Measurement and mitigation of the ionosphere in L-band interferometric SAR data. In Proceedings of the 2010 IEEE Radar Conference, Washington, DC, USA, 10–14 May 2010; pp. 1459–1463.
25. Schneider, R.; Papathanassiou, K. Ionospheric correction by means of coherent scatterers. In Proceedings of the European Conference on Synthetic Aperture Radar (EUSAR), Friedrichshafen, Germany, 2–5 June 2008.
26. Gomba, G.; Parizzi, A.; De Zan, F.; Eineder, M.; Bamler, R. Toward operational compensation of ionospheric effects in SAR interferograms: The split-spectrum method. *IEEE Trans. Geosci. Remote Sens.* **2015**, *54*, 1446–1461. [CrossRef]
27. Gomba, G.; González, F.R.; De Zan, F. Ionospheric phase screen compensation for the Sentinel-1 TOPS and ALOS-2 ScanSAR modes. *IEEE Trans. Geosci. Remote Sens.* **2016**, *55*, 223–235. [CrossRef]
28. Fattahi, H.; Simons, M.; Agram, P. InSAR time-series estimation of the ionospheric phase delay: An extension of the split range-spectrum technique. *IEEE Trans. Geosci. Remote Sens.* **2017**, *55*, 5984–5996. [CrossRef]
29. Zhang, B.; Wang, C.; Ding, X.; Zhu, W.; Wu, S. Correction of Ionospheric Artifacts in SAR Data: Application to Fault Slip Inversion of 2009 Southern Sumatra Earthquake. *IEEE Trans. Geosci. Remote Sens. Lett.* **2018**, *15*, 1327–1331. [CrossRef]
30. Liang, C.; Agram, P.; Simons, M.; Fielding, E.J. Ionospheric Correction of InSAR Time Series Analysis of C-band Sentinel-1 TOPS Data. *IEEE Trans. Geosci. Remote Sens.* **2019**, *57*, 6755–6773. [CrossRef]
31. Brcic, R.; Eineder, M.; Bamler, R. Interferometric absolute phase determination with terrasar-x wideband sar data. In Proceedings of the IEEE Radar Conference, Wessling, Germany, 4 August 2009; pp. 1–6.
32. Raucoules, D.; Michele, M.D. Assessing ionospheric influence on L-band SAR data: Implications on coseismic displacement measurements of the 2008 Sichuan earthquake. *IEEE Trans. Geosci. Remote Sens. Lett.* **2010**, *7*, 286–290. [CrossRef]
33. Chen, J.Y.; Zebker, H.A. Ionospheric artifacts in simultaneous L-band InSAR and GPS observations. *IEEE Trans. Geosci. Remote Sens.* **2012**, *50*, 1227–1239. [CrossRef]
34. Jung, H.S.; Lee, D.T.; Lu, Z.; Won, J.S. Ionospheric Correction of SAR Interferograms by Multiple-Aperture Interferometry. *IEEE Trans. Geosci. Remote Sens.* **2013**, *51*, 3191–3199. [CrossRef]
35. Liu, Z.; Jung, H.S.; Lu, Z. Joint correction of ionosphere noise and orbital error in L-band SAR interferometry of interseismic deformation in southern California. *IEEE Trans. Geosci. Remote Sens.* **2014**, *52*, 3421–3427. [CrossRef]
36. Zhang, B.; Ding, X.; Zhu, W.; Wang, C.; Zhang, L.; Liu, Z. Mitigating Ionospheric Artifacts in Coseismic Interferogram Based on Offset Field Derived From ALOS-PALSAR Data. *IEEE J. Sel. Top. Appl. Earth Obs. Remote Sens.* **2016**, *9*, 3050–3059. [CrossRef]

37. Freeman, A. Calibration of linearly polarized polarimetric SAR data subject to Faraday rotation. *IEEE Trans. Geosci. Remote Sens.* **2004**, *42*, 1617–1624. [CrossRef]
38. Kimura, H. Calibration of polarimetric palsar imagery affected by faraday rotation using polarization orientation. *IEEE Trans. Geosci. Remote Sens.* **2009**, *47*, 3943–3950. [CrossRef]
39. Sandberg, G.; Eriksson, L.; Ulander, L. Measurements of Faraday Rotation Using Polarimetric PALSAR Images. *IEEE Trans. Geosci. Remote Sens. Lett.* **2009**, *6*, 142–146. [CrossRef]
40. Takeshiro, A.; Furuya, T.; Fukuchi, H. Verification of polarimetric calibration method including Faraday rotation compensation using PALSAR data. *IEEE Trans. Geosci. Remote Sens.* **2009**, *47*, 3960–3968. [CrossRef]
41. Li, L.; Zhang, Y.; Dong, Z.; Liang, D. New faraday rotation estimators based on polarimetric covariance matrix. *IEEE Trans. Geosci. Remote Sens. Lett.* **2014**, *11*, 133–137. [CrossRef]
42. Rogers, N.C.; Quegan, S. The accuracy of Faraday rotation estimation in satellite synthetic aperture radar images. *IEEE Trans. Geosci. Remote Sens.* **2014**, *52*, 4799–4807. [CrossRef]
43. Kim, J.S.; Papathanassiou, K.P.; Quegan, S.; Rogers, N. Estimation and correction of scintillation effects on spaceborne P-band SAR images. In Proceedings of the 2012 IEEE International Geoscience and Remote Sensing SymposiumI (GARSS), Munich, Germany, 22–27 July 2012; pp. 5101–5104.
44. Kim, J.S. Development of Ionosphere Estimation Techniques for the Correction of SAR Data. Ph.D. Thesis, Eidgenössische Technische Hochschule ETH Zürich, Zurich, Switzerland, 2013.
45. Zhu, W.; Ding, X.L.; Jung, H.S.; Zhang, Q. Mitigation of ionospheric phase delay error for SAR interferometry: An application of FR-based and azimuth offset methods. *Remote Sens. Lett.* **2017**, *8*, 58–67. [CrossRef]
46. Lee, J.S.; Pottier, E. *Polarimetric Radar Imaging From Basics to Applications*; CRC Press: Boca Raton, FL, USA, 2009.
47. Quegan, S.; Lamont, J. Ionospheric and tropospheric effects on synthetic aperture radar performance. *Int. J. Remote Sens.* **1986**, *7*, 525–539. [CrossRef]
48. Xu, Z.W.; Wu, J.; Wu, Z.S. A survey of ionospheric effects on space-based radar. *Waves Random Media* **2004**, *14*, 189–272. [CrossRef]
49. Blewitt, G. An automatic editing algorithm for GPS data. *Geophys. Res. Lett.* **1990**, *17*, 199–202. [CrossRef]
50. Shimada, M.; Isoguchi, O.; Tadono, T.; Isono, K. PALSAR radiometric and geometric calibration. *IEEE Trans. Geosci. Remote Sens.* **2009**, *47*, 3915–3932. [CrossRef]
51. Baran, I.; Stewart, M.; Kampes, B.; Perski, Z.; Lilly, P. A modification to the Goldstein radar interferogram filter. *IEEE Trans. Geosci. Remote Sens.* **2003**, *41*, 2114–2118. [CrossRef]
52. Finlay, C.; Maus, S.; Beggan, C.; Bondar, T.; Chambodut, A.; Chernova, T.; Chulliat, A.; Golovkov, V.P.; Hamilton, B.; Hamoudi, M.; et al. International geomagnetic reference field: The eleventh generation. *Geophys. J. Int.* **2010**, *183*, 1216–1230.
53. Costantini, M.; Rosen, P.A. A generalized phase unwrapping approach for sparse data. In Proceedings of the IEEE 1999 International Geoscience and Remote Sensing SymposiumI (GARSS), Hamburg, Germany, 28 June–2 July 1999; pp. 267–269.